nuclear fusion
IAEA

PAPER • OPEN ACCESS

Correlation between radiated power and target heat flux in the island divertor of W7-X

To cite this article: G. Partesotti *et al* 2026 *Nucl. Fusion* **66** 026021

View the article online for updates and enhancements.

You may also like

- Core plasma fueling by fast inward particle transport after hydrogen pellet injection in Wendelstein 7-X
H. Damm, J. Baldzuhn, R.C. Wolf et al.
- On the possibility of reducing the size of a fusion reactor by increasing the plasma density
C. Angioni, E. Fable and H. Zohm
- Model-based estimation of tokamak plasma profiles and physics parameters: integration with improved equilibrium reconstruction and experimental data
S. Van Mulders, S.C. McIntosh, F. Carpanese et al.

This content was downloaded from IP address 94.31.113.212 on 06/02/2026 at 14:40

OPEN ACCESS
IOP Publishing | International Atomic Energy Agency
Nuclear Fusion
Nucl. Fusion **66** (2026) 026021 (13pp)
https://doi.org/10.1088/1741-4326/ae2af3

Correlation between radiated power and target heat flux in the island divertor of W7-X

G. Partesotti[1,*], F. Reimold[1], G.A. Wurden[2], N. Maaziz[1], A. Tsikouras[1], B.J. Peterson[3], F. Federici[4], K.A. Siever[1], A. Puig Sitjes[1], M. Jakubowski[1], Y. Gao[1], T. Nishizawa[5], K. Mukai[3] and the W7-X Team[a]

[1] Max-Planck Institute for Plasma Physics, Greifswald, Germany
[2] Los Alamos National Laboratory, Los Alamos, NM, United States of America
[3] National Institute for Fusion Science, Toki, Japan
[4] Oak Ridge National Laboratory, Oak Ridge, TN, United States of America
[5] Research Institute for Applied Mechanics, Kyushu University, Kasuga, Japan

E-mail: gabriele.partesotti@ipp.mpg.de

Received 29 August 2025, revised 2 December 2025
Accepted for publication 10 December 2025
Published 6 January 2026

Abstract

Radiative losses from the plasma represent a key component of global power balance in a magnetic confinement fusion device. Measurements of the plasma radiation and its spatial distribution are essential for physical studies and to ensure safe machine operation. Here, an imaging bolometer diagnostic is employed to characterize the plasma radiated power in the island divertor of the large Wendelstein 7-X (W7-X) stellarator device. In attached plasmas, the divertor radiation pattern exhibits magnetic field-aligned stripes and a toroidally non-uniform character highly correlated with the target power load deposition pattern of the given magnetic field configuration. Toroidal uniformity of the plasma emissivity is partly recovered in detached discharges. Similar results are found in EMC3-EIRENE simulations of carbon impurity radiation, which indicate that the steep toroidal emissivity gradients observed in the experiment (factor $\times 2$ change over 10 cm parallel distance) are supported by toroidally localized particle sources.

Keywords: bolometry, IRVB, divertor, radiated power, thermography

(Some figures may appear in colour only in the online journal)

[a] See Grulke *et al* 2024 (https://doi.org/10.1088/1741-4326/ad2f4d) for the W7-X Team.
[*] Author to whom any correspondence should be addressed.

Original Content from this work may be used under the terms of the Creative Commons Attribution 4.0 licence. Any further distribution of this work must maintain attribution to the author(s) and the title of the work, journal citation and DOI.

1. Introduction

Power exhaust is an ongoing challenge for magnetic confinement fusion devices [1]. One possible solution is the establishment of a highly radiative, detached plasma regime [2]. Radiation detachment can be employed to safeguard the divertor components from excessive heat/particle loads while maintaining high fusion performance [3]. At W7-X, controlled detached operation has been demonstrated both by means of impurity seeding [4] and main gas density fueling [5]. A proxy for the total plasma radiated power, here called $P_{\mathrm{rad}}^{\mathrm{cor}}$, is conventionally extracted from a local measurement performed by the Horizontal Bolometer Camera (HBCm) [6]. This consists of an array of resistive metal foil bolometers measuring from the outboard side of one triangular plane with a symmetrical layout [7]. The extrapolation is based on the assumption of toroidally uniform plasma emissivity, which might be partially invalid in some scenarios [8].

To test the toroidal symmetry of the radiation distribution, the bolometry system was extended by installing an InfraRed Video Bolometer (IRVB) diagnostic in the divertor region of W7-X. An overview of the diagnostic design and operating principle at W7-X can be found in [9]. The IRVB concept was developed and implemented at LHD [10–14]. Like traditional resistive bolometers, it yields a measurement of the radiative power losses from the plasma, line-integrated within each bolometer sightline [10]. However, the IRVB offers a relatively higher number of channels and a wider detection volume. The W7-X IRVB diagnostic provides a direct view on the target plates of one upper divertor unit [15] and allows for characterization of the plasma radiated power in the target interaction region of the W7-X island divertor [16, 17].

First, the diagnostic design is introduced in section 2. Then, the experimental observations are reported in section 3 with the aid of tomographic reconstructions and wall thermography data. Finally, section 4 reports some synthetic results simulated using the EMC3-EIRENE code [18].

2. The IRVB diagnostic

The active detection volume offered by the IRVB diagnostic at W7-X is visualized in orange color in figure 1(*a*). This is represented by the area subtended by the pinhole towards the bolometer detector foil. Relevant wall components (shield, baffle, closure, targets) are also rendered for reference. The resulting field-of-view (FoV) covers the upper portion of the plasma cross section, with the pinhole located near the toroidal angle $\varphi = 14°$ (teal and black solid lines) of module five. In the standard magnetic field configuration of W7-X, most of the heat flux is deposited in the shape of two main strike lines (see later figure 5(*a*)). These two are toroidally localized on the vertical target section (yellow) and on the low-iota section (indigo) of the horizontal target plate respectively [19, 20]. Hence, the IRVB images the area of the target plates where most of the standard power load deposition takes place. However, the IRVB coverage does not include the middle (blue) and high-iota (green) portion of the divertor unit, where the strike line is located in the high-iota configuration [21].

Bolometer channels are defined by partitioning the surface of the 2.5 μm-thick platinum foil into $33 \times 43 = 1419$ identical square pixels. Each identifies an individual line-of-sight (LoS) of the bolometer measurement. A view of the components from figure 1(*a*) projected onto the foil plane is reported in figure 1(*b*) to visualize the area covered by each bolometer channel in the W7-X machine. As indicated by the magnetic axis (white solid line), the toroidal (poloidal) direction is roughly aligned with the horizontal (vertical) dimension of the foil. Channels in the middle of the view sample the plasma volume in the direction of the vertical target plate, while the horizontal target plate occupies the upper portion of the view. The spatial resolution is measured as the distance between two adjacent central LoSs. This value is about 1.0 cm at the scrape-off layer (SOL) near the IRVB pinhole at the outboard side, while it increases to 5.0 cm on the further (inboard) side at the pumping gap due to the non-zero divergence of the LoSs.

3. Measurements

3.1. Resistive bolometers

All the following experimental analysis will be performed on one example ECR-heated discharge performed in the standard magnetic field configuration (XP:20241119.89), of which an overview is presented in figure 2. Following the startup phase, the plasma enters an attached phase at input ECRH power $P_{\mathrm{heat}} = 6.0\,\mathrm{MW}$ (black upper panel). During the time interval $t = 1.0\,\mathrm{s}$–$3.0\,\mathrm{s}$, the density ramp stops and the line-integrated density remains constant at $\int n_{\mathrm{e}}\,\mathrm{dl} = 10 \times 10^{19}\,\mathrm{m}^{-2}$ (blue lower panel). In this steady-state phase, the total radiated power measured at the triangular plane is stable at $P_{\mathrm{rad}}^{\mathrm{cor}} =$ 1.3 MW (red upper panel), giving a radiated power fraction of $f_{\mathrm{rad}} = P_{\mathrm{rad}}^{\mathrm{cor}}/P_{\mathrm{heat}} = 0.2$. Then, over one second ($t = 3.0$ s–4.0 s), the input heating power is stepped down to $P_{\mathrm{heat}} = 3.4$ MW and the line-integrated density is ramped to $\int n_{\mathrm{e}}\,\mathrm{dl} = 14 \times 10^{19}\,\mathrm{m}^{-2}$ by fueling from the main gas system. This causes the diamagnetic energy to drop from $W_{\mathrm{dia}} = 720\,\mathrm{kJ}$ to $W_{\mathrm{dia}} = 600$ kJ (black lower panel). Between $t = 4.0$ s–6.0 s (discharge termination), the plasma enters a steady-state detached phase and the total plasma radiated power measured by HBCm remains stable at $P_{\mathrm{rad}}^{\mathrm{cor}} = 3.2\,\mathrm{MW}$ ($f_{\mathrm{rad}} = 0.95$).

Tomographic inversions can provide additional information on the plasma radiation distribution in the 2D poloidal plane. The tomographic solution is found employing a newly developed Python routine based on Gaussian process tomography (GPT) [22]. This is applied to line-integrated experimental data acquired by a second bolometer diagnostic: the resistive divertor bolometry system [8]. This consists of an array of five resistive metal foil bolometer cameras (see later figure 7(*b*)) for a total of 93 sightlines: two viewing the lower divertor target plates ($28 + 20$ sightlines), and three viewing

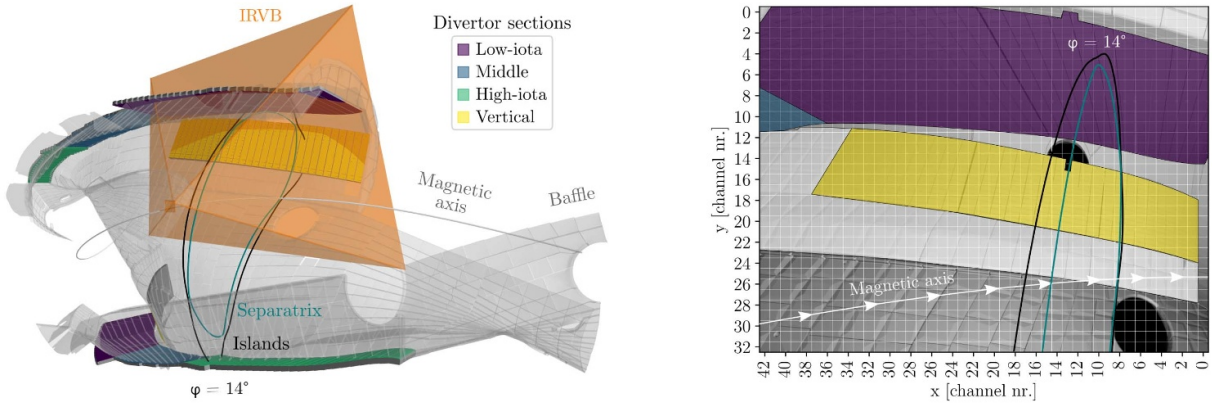

(a) 3D detection volume of the IRVB diagnostic

(b) IRVB view on the wall components

Figure 1. (*a*) Three-dimensional render of the IRVB detection volume (orange) and relevant W7-X wall components. Divertor closure, baffle, and shield are displayed in semitransparent gray color. Different sections of the divertor unit are highlighted with different colors. The standard magnetic geometry at $\varphi = 14^\circ$ is visualized with solid lines (teal separatrix, black islands). The magnetic axis is plotted as a white solid line. (*b*) FoV of the diagnostic projected in the foil plane. Channel numbers are noted on the plot axes. The positive direction of the magnetic field is indicated by white arrows on the magnetic axis. Black circles are diagnostic port holes.

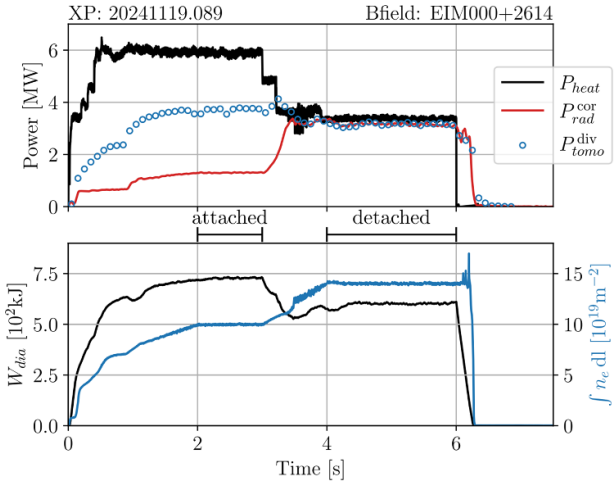

Figure 2. Overview of the standard configuration discharge XP:20241119.89. Upper: input ECRH power (black) and total radiated power measured at the triangular plane (red) and in the divertor region (blue). Lower: line-integrated density (blue) and diamagnetic energy (black).

the upper portion of the plasma and the high-iota tail of the upper divertor unit ($20 + 20 + 5$ sightlines).

Two tomographic reconstructions are generated from resistive divertor bolometry experimental data for the attached and detached phase of the discharge. The inversion plane is located at toroidal angle $\varphi = 58^\circ$, which is stellarator-equivalent to the $\varphi = 14^\circ$ plane (see figure 1) at the IRVB measurement location. Then, assuming stellarator symmetry, the two reconstructions can be flipped upside-down to obtain the expected poloidal radiation distribution within the IRVB FoV. The resulting tomograms are shown in figures 3(*a*) and (*b*) for the attached and detached phase of the discharge respectively. The chi-squared confidence factor χ^2 and is noted in the bottom-left corner of the tomogram plots [22].

Since detachment is achieved without impurity seeding, the (intrinsic) radiation pattern should be dominated by line radiation emitted by the carbon impurities released by the Plasma-Facing Components (PFCs) [6, 23]. Due to the large noise levels experienced by the resistive divertor bolometry system in the early phase of its deployment, the tomographic reconstructions presented here suffer from a number of artifacts and poorly localized radiation sources. This is especially true for the detached case (reflected in the lower χ^2 value). Still, the gross features and temporal behavior of the measured radiation are reliable and can be used for a qualitative analysis.

The reconstructed emissivity reveals two emission peaks located in the SOL above the surface of the upper divertor target plates in the attached phase (see figure 3(*a*)). Core radiation yields a comparatively minor contribution. At detachment, the resistive divertor bolometry system detects an intensification of the horizontal target radiation front relative to the vertical target radiation front and a movement towards the X-point above the pumping gap. However, the overall intensity of the radiation appears to reduce, which is in contrast with the total radiated power measurement presented in figure 2 (red).

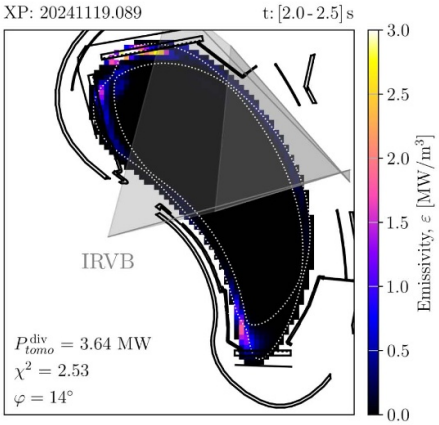

(a) Radiation tomogram (attached)

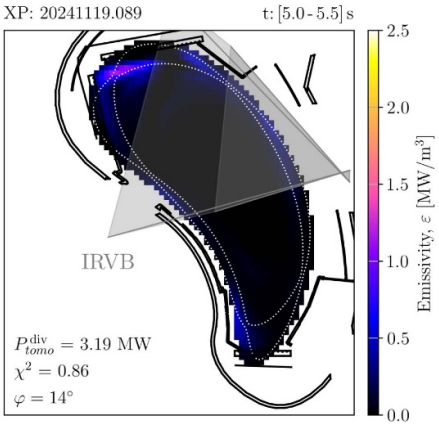

(b) Radiation tomogram (detached)

Figure 3. Tomographic reconstruction of the 2D poloidal radiation distribution in the (*a*) attached and (*b*) detached phase. The poloidal projection of the IRVB FoV is overlaid (gray), together with an outline of the standard magnetic islands (white dotted).

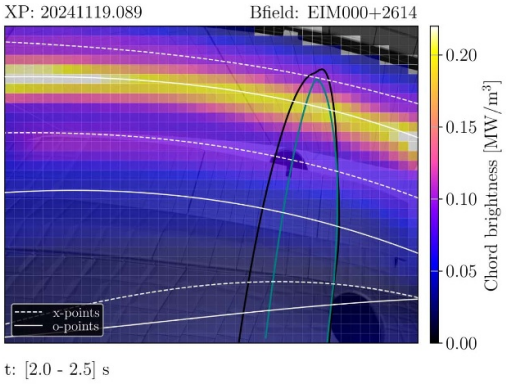

(a) Mapped line-averaged emissivity (attached)

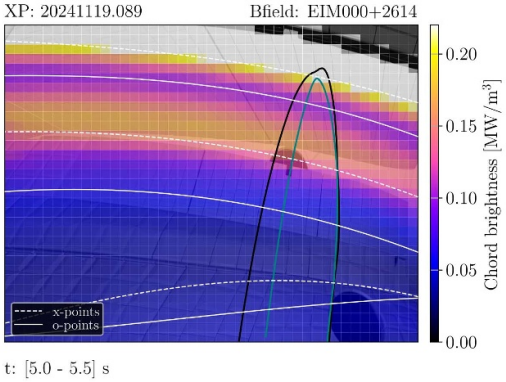

(b) Mapped line-averaged emissivity (detached)

Figure 4. Synthetic IRVB measurement of the plasma emissivity obtained by projecting the radiation distribution reconstructed in figures 3(*a*) and (*b*) onto the diagnostic FoV (assuming toroidally uniform emissivity). Discharge numbers and time intervals are noted on the upper and lower side of the frame.

To quantify the decrease in the peak plasma emissivity measured by the resistive divertor bolometry system following detachment, the radiated power reconstructed by the bolometry system is integrated throughout the volume, obtaining the tomographic estimate P^{div}_{tomo} [24]. This represents a second independent proxy for the total radiated power extracted from the local measurement in the divertor region, to be compared with the (traditional) geometrical proxy P^{cor}_{rad} extracted from the triangular plane. The tomographic estimate is noted on the bottom-left corner of each tomogram, and a time trace of P^{div}_{tomo} for the whole discharge is plotted as blue scatter points in the upper panel of figure 2.

In the attached phase, the two proxies deviate from each other as a significantly higher radiated power level $P^{div}_{rad} = 3.7$ MW is found in the divertor region than at the triangular plane. During the transition phase, the divertor radiated power lowers to $P^{div}_{tomo} = 3.2$ MW and P^{cor}_{rad} rises until the two estimates converge. This phenomenon is currently understood to be a consequence of toroidal redistribution of the plasma radiation that accompanies the increase in toroidal symmetry observed in the transition to detachment. The two proxies P^{cor}_{rad} (traditional) and P^{div}_{tomo} (novel) are considered as two independent and equally valid total radiated power values for two separate toroidal locations in the W7-X device. Combining them to obtain a more comprehensive assessment of global power balance will be the scope of future work.

Using the assumption of constant parallel emissivity, the radiation tomogram can be extended along the field lines and projected onto the FoV of the IRVB diagnostic [22]. The so-obtained synthetic data is shown in figures 4(*a*) and (*b*), overlaid with the island geometry of the original tomogram plane $\varphi = 14°$ (as in figure 1(*b*)). This represents the expected IRVB measurement from tomography (in ideally toroidally uniform radiation conditions), which will be compared with the experimental data later in section 3.3.

In this case, the line-integrated power incident on each IRVB channel is normalized to the individual channel geometry [9]. This is done to extract the line-averaged

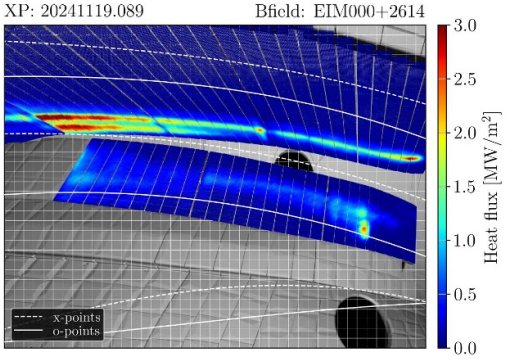

(a) Divertor target heat flux (attached)

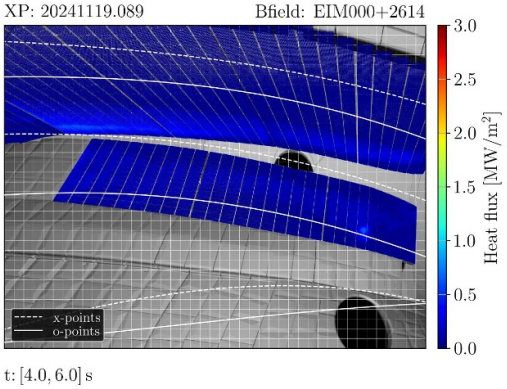

(b) Divertor target heat flux (detached)

Figure 5. Heat flux deposited on the divertor target surface from the wall thermography system in the (*a*) attached and (*b*) detached phase. The heat flux data is projected on the IRVB FoV.

emissivity information, also referred to as chord brightness $\varepsilon_{\mathrm{ch}}$ [Wm^{-3}] in the literature, which better represents the plasma emissivity features [6, 8]. To avoid saturating the signal, channels that do not intersect the plasma and channels with minimal etendue value are set to transparent in the plot (e.g. upper right corner of figures 4(*a*) and (*b*)). To better understand the magnetic field geometry in the SOL, a 3D trace of the magnetic island (black in figure 1(*a*)) X-points and O-points is projected onto the foil plane and plotted as dashed and solid white lines respectively.

3.2. Thermography

To complement the bolometric measurements, the plasma load on the divertor targets can be retrieved from the W7-X wall thermography system [25]. This involves using the THEODOR code to infer the heat flux deposited on the target surface from the infrared emission measured on the upper divertor unit imaged by IRVB [26, 27]. The heat flux calculated in the attached and detached plasma phase defined in figure 2 is presented figures 5(*a*) and (*b*) respectively. For better comparability, the heat flux data is visualized directly as it would be seen by the IRVB diagnostic. This mapping of the heat flux data is achieved by projecting the coordinates of each target element through the pinhole onto the foil plane, simulating the pinhole camera effect.

In attached conditions, the standard configuration power deposition pattern is characterized by two main strike lines: one on the vertical target plate and one on the low-iota section of the horizontal target plate [20]. During radiation detachment (figure 5(*b*)), the heat flux to the targets drops significantly. A faint band of power load ($< 0.5\,\mathrm{MWm}^{-2}$) remains visible on the target. Excluding artifacts, this could be a result of the radiated power fraction being non-unitary ($f_{\mathrm{rad}} = 0.95$), or direct radiation loads on the target surface [28]. Its presence might indicate that a small amount of recycling is still present at the target.

3.3. IRVB

The IRVB measurement averaged during the attached and detached phase of the plasma discharge is shown in figures 6(*a*) and (*b*) respectively. The coefficients utilized for the conversion from foil temperature to incident power were absolutely calibrated via laser radiation experiments [9]: heat conductivity $\kappa = 1.648 \times 10^{-6}\,\mathrm{m}^2\mathrm{s}^{-1}$, heat sensitivity

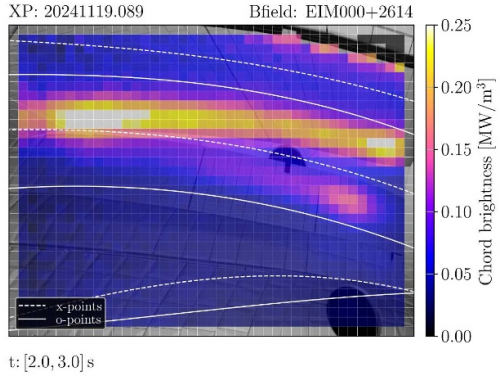

(a) Line-averaged emissivity (attached)

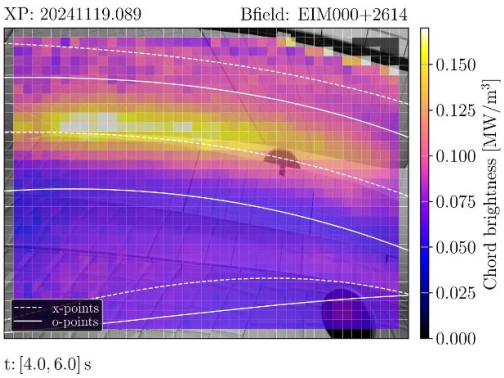

(b) Line-averaged emissivity (detached)

Figure 6. Plasma emissivity measured by IRVB during the (*a*) attached and (*b*) detached phase of the plasma discharge indicated in figure 2. The 3D traces of the island X-points (dashed) and O-points (solid) crossing the IRVB FoV are projected onto the foil plane as white lines.

$S = 1.457 \times 10^4$ KW^{-1}, emissivity $\varepsilon = 0.9$. The data is reported in units of chord brightness $\varepsilon_{\mathrm{ch}}$ as in figure 4.

In attached conditions, the radiation pattern measured by IRVB (figure 6(*a*)) is characterized by two main field-aligned radiation stripes. The stripe location with respect to the pumping gap and their width is well recovered in the synthetic pattern presented in figure 4(*a*). However, each radiation stripe imaged in the experiment exhibits significant toroidal emissivity gradients within the IRVB FoV. Since the synthetic data represents the case of ideal toroidal symmetry, the deviation between the mapped and measured image highlights the asymmetric character of the experimental measurements. In particular, the chord brightness measured by IRVB on the lower radiation band in a toroidally symmetric case should increase when moving from $\varphi = 14°$ (right) to $\varphi = 0°$ (left) due to the different plasma volume covered by the diagnostic. On the contrary, the experimentally measured chord brightness is found to decrease in the same region, indicating a toroidal radiated power gradient.

When compared to the distribution shown in figure 5(*a*), it can be noticed how the attached radiated power distribution is highly correlated with the power deposition pattern on the targets. This supports the idea that IRVB is imaging a three-dimensional radiation structure originating on the open field lines of the SOL near the region of plasma-target interaction [22, 29], which is in agreement with the tomographic data (see figure 3). Alternatively, the observed correlation could be a result of direct IR emission from the hot divertor surface. However, power deposition from thermal emission of a 300°C target element is expected to be of the order of 10 μW per bolometer channel. This is more than a factor $\times 10$ lower than the observed signal level at the strike line, and therefore negligible. At the same time, no significant shine-through of IR radiation was observed when placing the foil in front of a precision black-body source heated up to temperatures of 300°C [9]. These considerations indicate that the observed IRVB radiation pattern is indeed a feature of plasma volume emission and not of a thermal radiation source from the divertor target. A similar correlation between radiated power and heat flux distribution during the attached phase is found consistently in all W7-X magnetic field configurations observed so far. More examples in non-standard magnetic field configurations can be found in the appendix A.1.

Upon entering detachment (figure 6(*b*)), the radiation pattern becomes more toroidally uniform, and the correlation with the power deposition pattern is lost. The upper radiation stripe broadens and appears to intensify relative to the lower stripe [30]. Furthermore, two additional radiation bands appear inside the view in correspondence with the upper and lower X-point. The peak intensity measured by IRVB is reduced compared to the attached case as the radiation distribution becomes more diffused within the IRVB view, which is consistent with the toroidal redistribution effect observed in section 3.1. In this case, the synthetic data forward calculated under the assumption of constant parallel emissivity (see figure 4(*b*)) is more similar to the experimental measurement. The better agreement in terms of toroidal distribution indicates a reduction of the toroidal emissivity gradients in the detached phase of the experiment. For another example of improved toroidal symmetry, the reader is directed to the appendix A.2.

In the synthetic image of figure 4(*b*), a bright region appears on the upper side which is not present in the experiment. This originates from the SOL on the outboard side of the plasma (right-hand side of figure 3(*b*)). This is likely due to tomographic errors such as artifacts caused by noise or an incorrect prior model. Even a small amount of radiation placed here due to artifacts could lead to a large signal due to the long integration length. It must be pointed out that the tomographic solution is found assuming a constant parallel plasma emissivity within the toroidal range $\Delta\varphi = 8°$ covered by the resistive divertor bolometry system [8]. This assumption could be invalid given the toroidal gradients observed by IRVB. In addition, the assumption of stellarator symmetry between the lower (tomography) and upper (IRVB) divertor unit might not hold (e.g. due to drift effects) [31, 32].

To support the qualitative observations drawn from the comparison between figures 4 and 6, a quantitative metric for estimating the degree of toroidal uniformity within an IRVB image is defined. First, a reference synthetic IRVB measurement p_{ref} is generated from a forward calculation on an

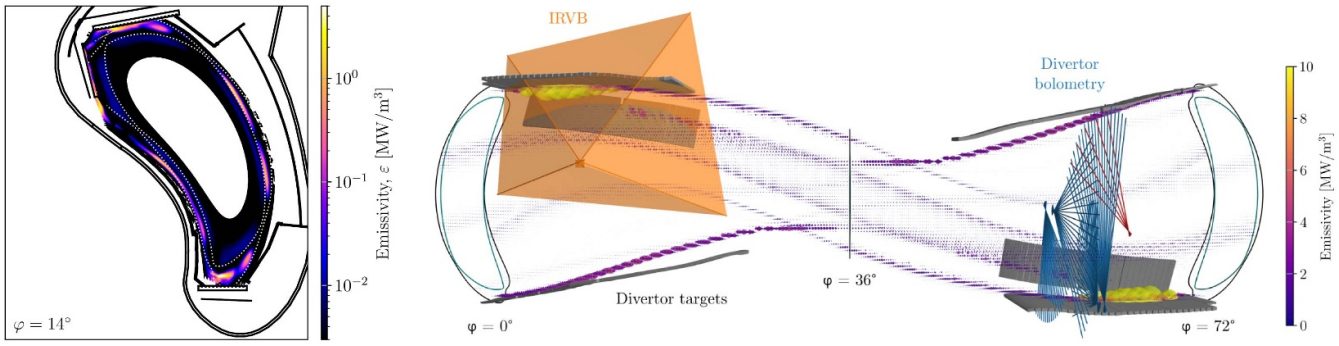

(a) Poloidal emissivity distribution

(b) 3D emissivity distribution of carbon impurity radiation

Figure 7. (*a*) Poloidal radiated power distribution of carbon impurity emission computed by EMC3-EIRENE at toroidal angle $\varphi = 14°$. (*b*) 3D emissivity distribution inside one W7-X module. The size of each scatter point is proportional to the local emissivity value. A render of the divertor target surfaces is included in gray color with the standard magnetic island geometry at angles $\varphi = 0°, 36°, 72°$ (teal separatrix, black islands). The IRVB (orange) and resistive divertor bolometry (blue and red) sightlines are overlaid.

ideally uniform radiation distribution. Then, the toroidal symmetry within each IRVB image can be quantified by computing the correlation between the experimentally measured radiated power pattern p and p_{ref} (over the whole image, both normalized). This exercise yields $\text{corr}(p, p_{\text{ref}}) = 2.2\%$ for the attached case and $\text{corr}(p, p_{\text{ref}}) = 4.8\%$ for the detached case, indicating again improved toroidal symmetry of the radiation during detachment.

4. Simulations

EMC3-EIRENE [18] simulations with carbon impurity radiation can provide a precious insight into the physical mechanisms that determine the radiated power distribution observed in the experiment. Here is presented an EMC3-EIRENE solution computed in the standard magnetic field configuration. The electron density at the separatrix is set to $n_{\text{sep}} = 3.0 \times 10^{19}\,\text{m}^{-3}$. Input heating power is $P_{\text{heat}} = 5.0\,\text{MW}$, while the content of carbon impurities is regulated to maintain a total radiated power of $P_{\text{rad}}^{\text{cor}} = 1.5\,\text{MW}$ (attached $f_{\text{rad}} = 0.3$). Anomalous transport is governed by the perpendicular particle diffusion coefficient $D_\perp = 0.2\,\text{m}^2\text{s}^{-1}$ and heat diffusion coefficient $\chi_\perp = 3D_\perp = 0.6\,\text{m}^2\text{s}^{-1}$. The low diffusion coefficients were shown to offer a better match to the experimental downstream plasma parameters [33].

Figure 7(*a*) reports the output spatial distribution of the plasma radiated power in the poloidal plane at $\varphi = 14°$. The simulated features are strongly localized (note the logarithmic color bar) and peak in the SOL between the island X-points and O-points [8, 29, 34]. The code respects stellarator symmetry within the simulation volume ($\varphi = 0° - 36°$). However, the plasma parameters are not necessarily conserved in the parallel direction, causing the emissivity to vary along the field line. The complete three-dimensional spatial distribution of radiated power inside one W7-X stellarator module is visualized in figure 7(*b*), alongside the sightlines of the IRVB diagnostic (orange) and the resistive divertor bolometry system (blue and red). The 3D render illustrates how the SOL radiation features shown in figure 7(*a*) connect other toroidal

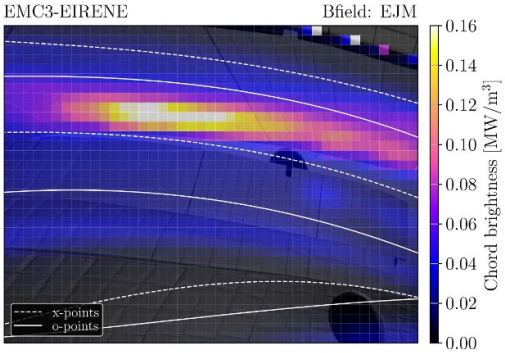

(a) Line-averaged emissivity (EMC3-EIRENE)

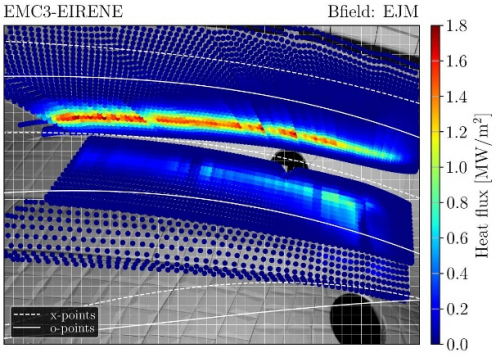

(b) Target heat flux (EMC3-EIRENE)

Figure 8. (*a*) Synthetic image of the IRVB chord brightness corresponding to the radiation distribution of figure 7(*b*). (*b*) Computed heat flux data projected on the IRVB FoV.

locations with varying intensity. In this case, the IRVB FoV at the upper divertor unit covers a region of peak intensity and steep spatial gradients.

Using a forward model for the IRVB diagnostic, a synthetic IRVB measurement is generated by projecting the 3D radiation distribution computed by EMC3-EIRENE onto each bolometer channel [8]. Figure 8(*a*) reports the associated line-averaged emissivity. Both toroidal peaking location

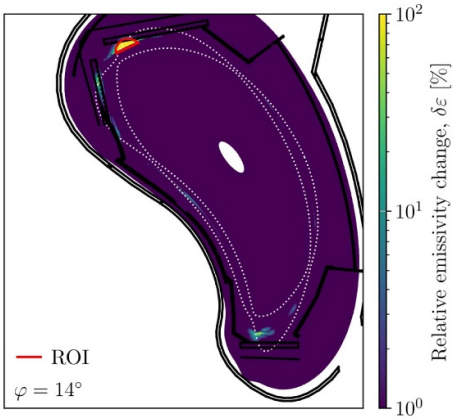

(a) Toroidal emissivity variation

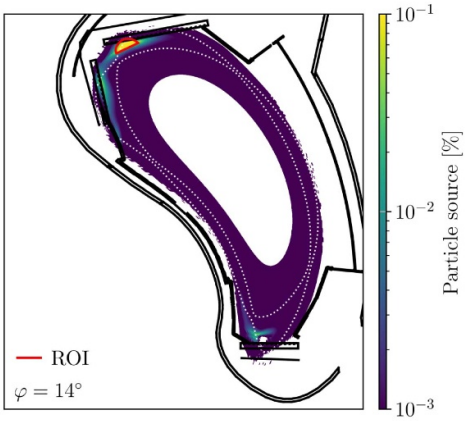

(b) Particle sources

Figure 9. (*b*) Toroidal emissivity variation $\delta\varepsilon$ within the simulation domain (normalized). (*c*) Particle sources summed up inside each flux tube. A red ROI identifies the flux tubes where $\delta\varepsilon > 75\%$.

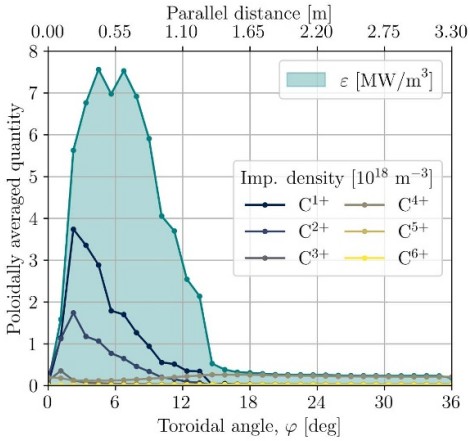

(a) Impurity density and radiation

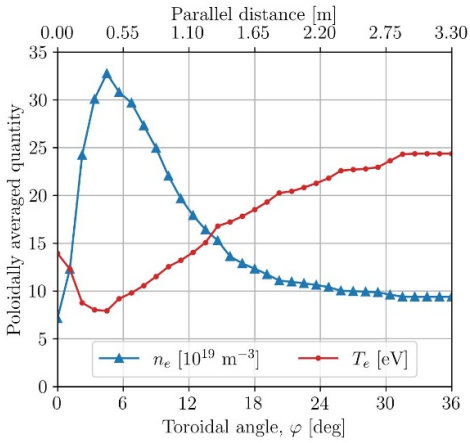

(b) Electron temperature and density

Figure 10. Toroidal profile of the plasma parameters computed by EMC3-EIRENE, poloidally averaged in the region of highest toroidal emissivity variation. (*a*) The plasma emissivity (teal fill) and the density of carbon impurity charge states (colored lines) vary considerably with toroidal angle. (*b*) The radiation peak is associated with a region of high electron density (blue) and low electron temperature (red).

of the emissivity (left-hand side) and toroidal gradients are comparable to experimental observations (see figure 6(*a*)). The correlation with the toroidal coordinate in this case is $\mathrm{corr}(p, p_{\mathrm{ref}}) = 2.0\%$. Similarly to the experiment, the synthetic emissivity measurement is reminiscent of the target heat flux pattern computed by EMC3-EIRENE, which is projected on the IRVB FoV in figure 8(*b*). However, the connection between the two is less evident.

The largest toroidal variation takes place inside the flux tubes intersecting the target at a close (order of one meter) parallel distance to the target plates. The emissivity deviation $\Delta\varepsilon = \max(\varepsilon) - \min(\varepsilon)$ is normalized to the average value inside the half-module $\delta\varepsilon = \Delta\varepsilon/\langle\varepsilon\rangle$ and expressed as a percentage. $\delta\varepsilon$ reaches its peak near the horizontal target plate, as shown in figure 9(*a*). This pattern of $\delta\varepsilon$ coincides with the region fed by the highest particle sources, whose poloidal distribution is summed toroidally and plotted in figure 9(*b*).

In this figure, a slight mismatch between the toroidal angle of the wall cut ($\varphi = 14°$) and of the EMC3-EIRENE mesh ($\varphi = 14.6°$) gives the impression that non-zero values of the emissivity and particle source are found inside the divertor material. In reality, all the cells visualized fall inside the plasma volume. Cells that belong to flux tubes that lie mostly or entirely inside materials are automatically discarded from the analysis.

A region of interest (ROI) is defined to focus the analysis on the plasma volume that exhibits the largest toroidal emissivity variation. This is done by selecting the flux tubes for which $\delta\varepsilon > 75\%$ (red in figure 9). At each toroidal angle, the plasma parameters inside this selected area are averaged poloidally. The toroidal profile of these poloidally averaged quantities is visualized below in figure 10.

Inside the ROI, a significant toroidal variation of the plasma parameters is observed. As shown in figure 10(*a*), the carbon impurity density (colored lines) is toroidally asymmetric. The non-uniform impurity concentration is sustained by particle sources originating from recycling [29]. Hence, the maximum

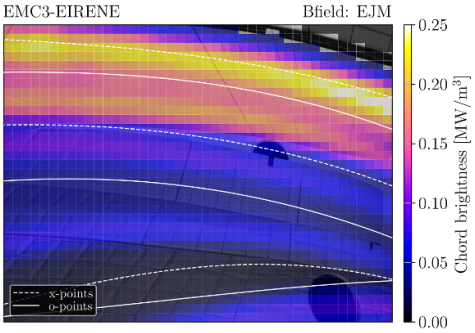

(a) Line-averaged emissivity (EMC3-EIRENE)

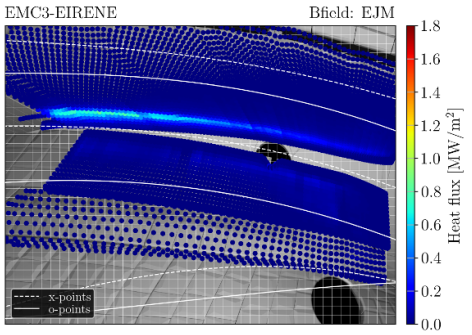

(b) Target heat flux (EMC3-EIRENE)

Figure 11. (*a*) Synthetic image of the IRVB chord brightness corresponding to the radiation distribution of figure 7(*b*). (*b*) Computed heat flux data projected on the IRVB FoV.

impurity density is localized in the toroidal range $\varphi = 0° - 18°$, where most of the plasma-target interaction takes place. This is accompanied by a local build-up of main ion density, as noticeable from the n_e profile shown in figure 10(*b*) (blue). In particular, the distribution of the lower impurity charge states (C^{1+} and C^{2+}, darker colors in figure 10(*a*)) is particularly localized. This indicates that the ionization mean free path of the carbon neutrals is short enough for them to start being ionized within the ROI and produce an ion source localized near the neutral particle source. At the same time, transport of the impurity ions is fast enough compared to their ionization rate, so carbon ions can penetrate relatively deeply into the plasma before being ionized further. This causes lowly ionized carbon ions to be found at higher temperatures than coronal equilibrium would allow. For example, coronal equilibrium predicts the abundance of the C^{1+} and C^{2+} charge states to peak at about $T_e = 1.0\,\text{eV}$ and $T_e = 5.0\,\text{eV}$ respectively, whereas in the EMC3-EIRENE solution their highest density is found at $T_e = 7.0$–$10.0\,\text{eV}$ [35]. Under these conditions, their emissivity is strongly increased [36].

The three-fold contribution of higher impurity density, electron density, and non-coronal effects gives rise to a localized enhancement of the plasma radiative efficiency in the recycling region. This is reflected in the toroidal profile of radiated power (teal fill in figure 10(*a*)): its intensity varies by up to a factor $\times 10$ across the half-module and peaks giving rise to a peak in the radiated power at $\varphi = 5°$. The resulting volumetric cooling effect leads to a drop in the local temperature T_e (red in figure 10(*b*)) and a further build-up of density supported by pressure conservation along the field line.

The simulated behavior is consistent with the radiation features observed in the experiment and reported in figures 6 and 12. The combination of IRVB, thermography, and tomography data indicates that radiative power losses in the island divertor are characterized by a fully three-dimensional distribution. The consequence is a non-uniform power dissipation inside the stellarator module, with significant implications for the exhaust capability of the machine and global power balance assessments [24]. In the poloidal plane, the emissivity of the 3D attached radiating structure peaks near the target plates, slightly lifted from the target surface. This is currently understood to be due to the dominant role of particle source effects to the radiative efficiency on the open field lines [29]: sputtering and recycling at the strike point lead to a localized buildup of impurity and main gas ions, dictating the observed toroidal gradients. Hence, the radiation peak is toroidally localized to the region of highest power/particle flux, as evident from the similarity between radiated power measured by IRVB and heat flux measured by thermography (see figure 6).

Finally, figure 11(*a*) reports the synthetic IRVB measurement of a detached EMC3-EIRENE solution. In this case, the same mesh and all plasma parameters as in figure 7(*b*) are employed, but the radiated power fraction is increased to $f_{rad} = 0.8$ by adjusting the impurity content. Compared to the attached case of figure 8(*a*), the detached data exhibits higher toroidal symmetry of the radiated power pattern, consistently

with the experiment (see figures 6(*a*) and (*b*)). Again, the emissivity near the upper and lower X-points is enhanced. The correlation factor with the reference uniform pattern in this detached simulation is only slightly higher, at $\mathrm{corr}(p, p_{\mathrm{ref}}) = 2.4\%$.

According to the higher radiated power fraction, the heat flux to the target is reduced on both target plates. However, two fainter bands of power deposition $< 0.6\,\mathrm{MWm}^{-2}$ remain visible, as shown in figure 11(*b*). During detachment, there is again a lower correlation between radiated power and target heat flux, which is in agreement with experimental results. However, the radiation intensity computed by EMC3-EIRENE is expected to increase at detachment (notice the different color bar between figures 8(*a*) and 11(*a*)), while the opposite behavior is observed in the experiment. Investigating this toroidal radiation redistribution effect and its modeling will be the scope of future work.

5. Conclusions

Recent experimental data from the newly installed IRVB diagnostic was used to characterize the plasma radiated power distribution in the island divertor. In particular, the IRVB is able to resolve toroidal gradients thanks to its wide FoV. A clear correlation between target heat flux and radiated power was consistently found in attached plasma conditions. The SOL divertor radiation features were found to be toroidally localized near the region of peak power load deposition. This is consistent with tomographic reconstructions performed on an independent (resistive) divertor bolometry system. The toroidal uniformity of the SOL plasma emissivity imaged by IRVB was found to increase during radiation detachment, as indicated by both qualitative and quantitative assessments using toroidal mapping and a toroidal correlation factor. Similar results were obtained from EMC3-EIRENE simulations of carbon impurity radiation. A factor $\times 10$ variation in the parallel plasma emissivity was calculated for the flux tubes magnetically connected to the divertor target plate at a short parallel distance. The emissivity peak was justified by a significant density buildup of main ions and impurities and non-coronal enhancement of the carbon radiative efficiency.

Data availability statement

The data that support the findings of this study are available from the corresponding author upon reasonable request

Acknowledgments

This work has been carried out within the framework of the EUROfusion Consortium, funded by the European Union via the Euratom Research and Training Programme (Grant Agreement No. 101052200—EUROfusion). Views and opinions expressed are however those of the author(s) only and do not necessarily reflect those of the European Union or the European Commission. Neither the European Union nor the European Commission can be held responsible for them.

This work was supported by the U.S. Department of Energy at Los Alamos National Laboratory, operated by Triad National Security LLC, for the National Nuclear Security Administration (Contract No. 89233218CNA000001).

This research was supported by the NINS-DAAD International Personal Exchange Program, JSPS Grant # 22KK0039, NIFS Grant # SIU004 and for B. J. Peterson the Alfried Krupp Wissenschaftskolleg Greifswald underwritten by the Stiftung Alfried Krupp Kolleg and the Alfried Krupp von Bohlen und Halbach-Stiftung.

This work is supported by US Department of Energy, Office of Fusion Energy Sciences under the Spherical Tokamak program, contract DE-AC05-00OR22725.

Appendix

A.1. Non-standard configurations

Figure 12 shows a comparison between the line-averaged emissivity from IRVB (upper) and the power load deposition pattern (lower) for three configurations of the W7-X magnetic field configurations: low-iota (left), high-mirror (center), and low-mirror (right). These refer to field geometries respectively with a lower iota (i.e. rotational transform, inverse of the safety factor), or higher/lower mirror ratio with respect to the W7-X standard configuration [21]. They are chosen for their markedly different pattern of power deposition inside the IRVB FoV. Respectively, this is mostly limited to the horizontal target, the vertical target, and the horizontal target at a closer distance to the pumping gap. Due to a lack of thermography data, the heat flux for figure 12(*c*) is currently not available. Instead, the heat flux shown in figure 12(*f*) is computed for another discharge with comparable plasma parameters (input power, line-integrated density, radiated power, magnetic configuration).

A.2. Small plasmas

Small plasma scenarios provide a good example of improved toroidal symmetry since they offer a steady-state radiation pattern that is entirely limited to the confined volume [22, 37]. As shown in figure 13(*a*), the poloidal radiation distribution of a small plasma presents a geometrically simple, flux-surface aligned hollow radiation ring. Being a radiation-limited regime, the heat flux reaching the target is approximately null ($<0.2\,\mathrm{MWm}^2$ everywhere) since the radiated power fraction is unitary and the radiation is more uniformly distributed. The toroidal uniformity of line-averaged emissivity measured by IRVB is remarkable, as noticeable from figure 13(*b*). For comparison, a toroidally symmetric synthetic IRVB measurement is generated from the tomographic reconstruction following the same logic as before. The result is plotted in figure 13(*c*). Measured and mapped image show good agreement both in terms of location of the radiation front and toroidal radiation distribution, demonstrating the toroidally symmetric character of the small plasma radiation. This is proven by the correlation between the measured power and the uniform reference $\mathrm{corr}(p, p_{\mathrm{ref}}) = 6.3\%$, which is higher

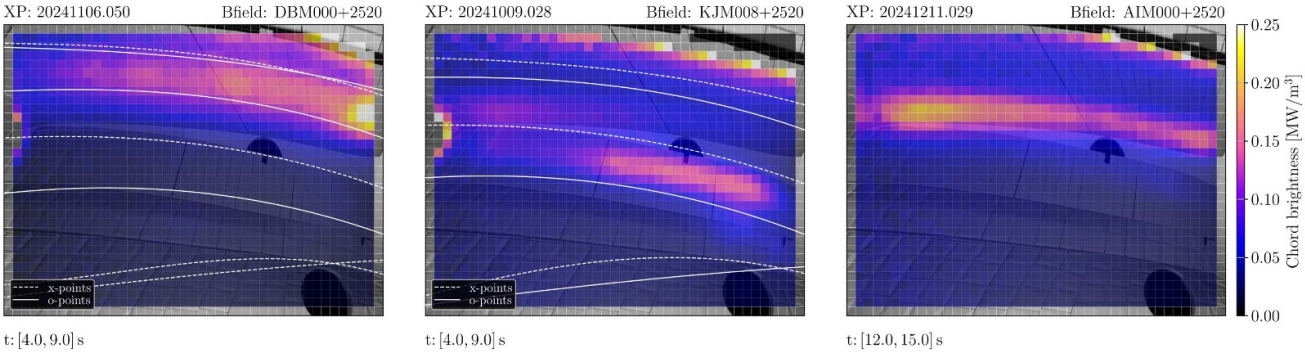

(a) Line-averaged emissivity (low-iota) (b) Line-averaged emissivity (high-mirror) (c) Line-averaged emissivity (low-mirror)

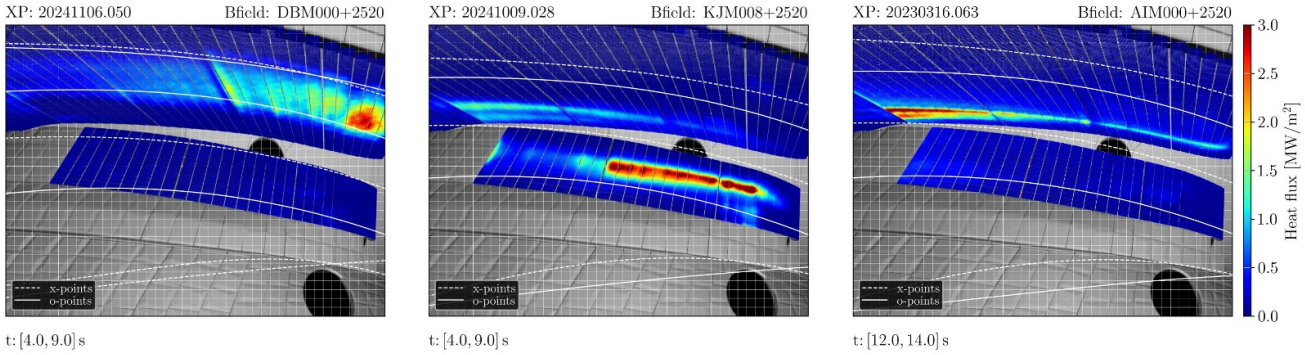

(d) Divertor target heat flux (low-iota) (e) Divertor target heat flux (high-mirror) (f) Divertor target heat flux (low-mirror)

Figure 12. Line-averaged emissivity measured by IRVB during a steady-state attached phase in the (*a*) low-iota, (*b*) high-mirror, and (*c*) low-mirror magnetic field configuration. The associated total radiated power in all cases is about $P_{\mathrm{rad}}^{\mathrm{cor}} = 1.0\,\mathrm{MW}$. (*d*)–(*f*) Corresponding divertor heat flux computed using THEODOR. (*f*) Is computed for a plasma discharge at comparable plasma parameters due to the lack of more recent thermography data.

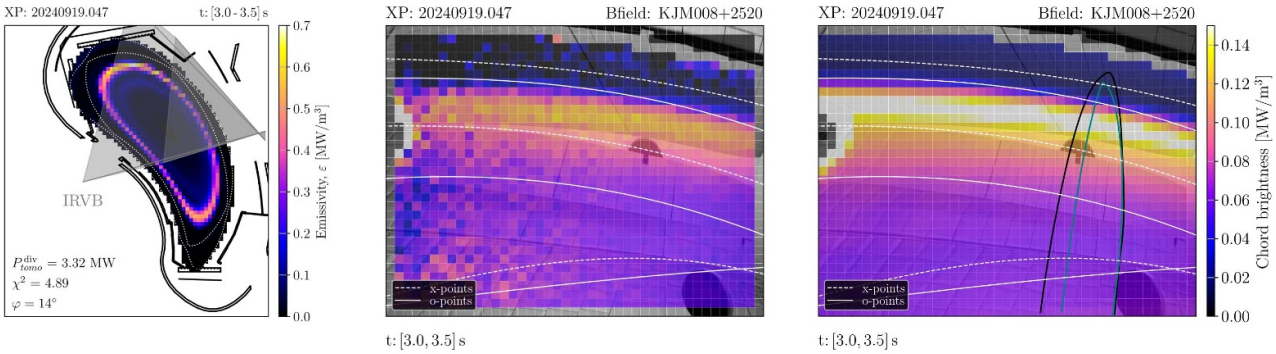

(a) Radiation tomogram (b) Line-averaged emissivity (measured) (c) Line-averaged emissivity (mapped)

Figure 13. (*a*) A tomographic reconstruction of the poloidal radiation distribution during a small plasma event. The (*b*) line-averaged emissivity measured by IRVB is compared to the one (*c*) mapped to the IRVB FoV from the tomogram. The standard magnetic island geometry at $\varphi = 14°$ is overlaid for reference as in figure 1(*b*).

than both the attached and the detached phase of the plasma discharge analyzed in section 3. The magnitude of the plasma emissivity differs by $\pm 10\%$, which could be due to calibration errors.

ORCID iDs

G. Partesotti 0009-0008-9465-7885
F. Reimold 0000-0003-4251-7924
G.A. Wurden 0000-0003-2991-1484
N. Maaziz 0009-0007-4199-5701
A. Tsikouras 0009-0008-9677-3302
B.J. Peterson 0009-0002-8230-0121
F. Federici 0000-0002-9354-7309
K.A. Siever 0009-0004-6365-6450
M. Jakubowski 0000-0002-6557-3497
Y. Gao 0000-0001-8576-0970
T. Nishizawa 0000-0003-1804-2308
K. Mukai 0000-0003-1586-1084

References

[1] ITER Physics Expert Group on Divertor, ITER Physics Expert Group on Divertor Modelling and Database and ITER Physics Basis Editors 1999 Chapter 4: power and particle control *Nucl. Fusion* **39** 2391
[2] Feng Y. *et al* 2021 Understanding detachment of the W7-X island divertor *Nucl. Fusion* **61** 086012
[3] Pitts R.A. *et al* 2019 Physics basis for the first ITER tungsten divertor *Nucl. Mater. Energy* **20** 100696
[4] Krychowiak M. *et al* 2023 First feedback-controlled divertor detachment in W7-X: experience from TDU operation and prospects for operation with actively cooled divertor *Nucl. Mater. Energy* **34** 101363
[5] Schmitz O. *et al* 2020 Stable heat and particle flux detachment with efficient particle exhaust in the island divertor of Wendelstein 7-X *Nucl. Fusion* **61** 016026
[6] Zhang D. *et al* 2021 Bolometer tomography on Wendelstein 7-X for study of radiation asymmetry *Nucl. Fusion* **61** 116043
[7] Zhang D. *et al* 2010 Design criteria of the bolometer diagnostic for steady-state operation of the W7-X stellarator *Rev. Sci. Instrum.* **81** 4
[8] Partesotti G., Reimold F., Ruhnau J., Tsikouras A., Kubeneck D., Zhang D. and Geißler P. 2024 Development of a compact bolometer camera concept for investigation of radiation asymmetries at Wendelstein 7-X *Rev. Sci. Instrum.* **95** 103503
[9] Partesotti G., Wurden G.A., Reimold F., Peterson B.J., Federici F., Mukai K., Siever K.A., von Miller J., Zhang D. and Demby A. 2025 The infrared imaging video bolometer at Wendelstein 7-X *Rev. Sci. Instrum.* **96** 063503
[10] Peterson B.J. 2000 Infrared imaging video bolometer *Rev. Sci. Instrum.* **71** 3696–701
[11] Sano R., Peterson B.J., Teranishi M., Iwama N., Kobayashi M., Mukai K. and Pandya S.N. 2016 Three-dimensional tomographic imaging for dynamic radiation behavior study using infrared imaging video bolometers in large helical device plasma *Rev. Sci. Instrum.* **87** 053502
[12] Mukai K., Abe R., Peterson B.J. and Takayama S. 2018 Improvement of infrared imaging video bolometer for application to deuterium experiment on the large helical device *Rev. Sci. Instrum.* **89** 10E114
[13] Mukai K., Kawamura G., Masuzaki S., Hayashi Y., Tanaka H., Peterson B.J., Oishi T., Suzuki C., Kobayashi M. and Munechika K. 2022 Three-dimensional structure of radiative cooling in impurity seeded plasmas in the Large Helical Device *Nucl. Mater. Energy* **33** 101294
[14] Munechika K., Tsutsui H., Peterson B.J., Mukai K., Kawamura G., Zhang D., Reimold F. and Partesotti G. 2025 Development of a 3-D tomography technique for large helical device bolometry using EMC3-eirene grids *Rev. Sci. Instrum.* **96** 043509
[15] Boscary J., Ehrke G., Greuner H., Junghanns P., Li C., Mendelevitch B., Springer J. and Stadler R. 2021 Completion of the production of the W7-X divertor target modules *Fusion Eng. Des.* **166** 112293
[16] Feng Y., Sardei F., Grigull P., McCormick K., Kisslinger J., Reiter D. and Igitkhanov Y. 2002 Transport in island divertors: physics, 3D modelling and comparison to first experiments on W7-AS *Plasma Phys. Control. Fusion* **44** 611
[17] Feng Y., Sardei F., Grigull P., McCormick K., Kisslinger J. and Reiter D. 2006 Physics of island divertor plasmas in stellarators *Contrib. Plasma Phys.* **46** 504–14
[18] Feng Y. *et al* 2014 Recent improvements in the EMC3-Eirene code *Contrib. Plasma Phys.* **54** 426–31
[19] Renner H., Boscary J., Greuner H., Grote H., Hoffmann F.W., Kisslinger J., Strumberger E. and Mendelevitch B. 2002 Divertor concept for the W7-X stellarator and mode of operation *Plasma Phys. Control. Fusion* **44** 1005
[20] Jakubowski M. *et al* 2021 Overview of the results from divertor experiments with attached and detached plasmas at Wendelstein 7-X and their implications for steady-state operation *Nucl. Fusion* **61** 106003
[21] Andreeva T. *et al* 2022 Magnetic configuration scans during divertor operation of Wendelstein 7-X *Nucl. Fusion* **62** 026032
[22] Partesotti G., Reimold F., Wurden G., Peterson B., Zhang D. and Mukai K. 2024 Assessing the toroidal radiation distribution at Wendelstein 7-X by combining Gaussian Process Tomography and field line mapping *Nucl. Mater. Energy* **41** 101823
[23] Zhang D. *et al* 2021 Plasma radiation behavior approaching high-radiation scenarios in W7-X *Nucl. Fusion* **61** 126002
[24] Partesotti G., Reimold F., Tsikouras A., Zhang D., Kawamura G. and Peterson B.J. 2024 Improved weighted sum estimation of total radiated power at W7-X *Nucl. Fusion* **65** 016035
[25] Jakubowski M. *et al* 2018 Infrared imaging systems for wall protection in the W7-X stellarator *Rev. Sci. Instrum.* **89** 10E116
[26] Herrmann A., Junker W., Gunther K., Bosch S., Kaufmann M., Neuhauser J., Pautasso G., Richter T. and Schneider R. 1995 Energy flux to the ASDEX-Upgrade diverter plates determined by thermography and calorimetry *Plasma Phys. Control. Fusion* **37** 17
[27] Gao Y., Jakubowski M.W., Drewelow P., Pisano F., Puig Sitjes A., Niemann H., Ali A. and Cannas B. 2019 Methods for quantitative study of divertor heat loads on W7-X *Nucl. Fusion* **59** 066007
[28] Maaziz N. and Reimold F. 2021 Improving power balance on Wendelstein 7-X *Technical Report* IPP 2024-10 (Max-Planck Institute for Plasma Physics)
[29] Winters V. *et al* 2024 First experimental confirmation of island SOL geometry effects in a high radiation regime on W7-X *Nucl. Fusion* **64** 126047
[30] Peterson B. *et al* 2025 Investigation of island size effect on radiation distribution during attached and detached plasmas in the island divertor of W7-X *Nucl. Mater. Energy* **42** 101868

[31] Hammond K.C. *et al* 2019 Drift effects on W7-X divertor heat and particle fluxes *Plasma Phys. Control. Fusion* **61** 125001
[32] Kriete D. *et al* 2023 Effects of drifts on scrape-off layer transport in W7-X *Nucl. Fusion* **63** 026022
[33] Bold D., Reimold F., Niemann H., Gao Y., Jakubowski M., Killer C., Winters V.R. and Maaziz N. 2024 Impact of spatially varying transport coefficients in EMC3-Eirene simulations of W7-X and assessment of drifts *Nucl. Fusion* **64** 126055
[34] Feng Y. *et al* 2024 Conditions and benefits of X-point radiation for the island divertor *Nucl. Fusion* **64** 086027
[35] Geißler P. 2022 Investigating radiation and its distribution in W7X with EMC3/Eirene *Technical Report* IPP 2024-26 (Max-Planck Institute for Plasma Physics)
[36] Roeltgen J., Kotschenreuther M., Harrison J., Moulton D., Chen Z.-P. and Mahajan S. 2022 Increased radiation due to non-coronal effects on DIII-D and MAST-U with varying input power *Nucl. Fusion* **63** 016013
[37] Pandey A. *et al* 2025 Stable small plasmas at the density limit in the W7-X stellarator *Phys. Rev. Lett.* **135** 175101